BIOMECHANICS OF THE ANTERIOR CRUCIATE LIGAMENT UNDER SIMULATED MOLECULAR DEGRADATION

M. Adouni[1,2,*], A. Gouissem[2], F. Al khatib[2] and A. Eilaghi[2]

[1] Northwestern University, Physical Medicine and Rehabilitation Department, 710 North Lake Shore Drive, Chicago, IL 60611, USA
[2] Australian College of Kuwait, Mechanical Engineering Department, East Mushrif, P.O. Box 1411, Kuwait

Abstract

Injuries to the knee anterior cruciate ligament (ACL) are common, with a known but poorly understood association with intrinsic and extrinsic risk factors. Some of these factors are enzymatically or mechanically mediated, creating acute focal injuries that may cause significant ligament damage. Understanding the relationship between the basic molecular structure and external loading of the ACL requires a hierarchical connection between the two levels. In the present study, a multi-domain frame was developed connecting the molecular dynamics of the collagen networks to the continuum mechanics of the ACL. The model was used to elucidate the effect of the two possible collagen degradation mechanisms on the aggregate ACL behaviour. Results indicated that collagen content and ACL stiffness were reduced significantly, regardless of the degradation mechanism. Furthermore, the volumetric degradation at the molecular level had a devastating effect on the mechanical behaviour of the ACL when it was compared with the superficial degradation. ACL damage initiation and propagation were clearly influenced by collagen degradation. To summarise, the new insights provided by the predicted results revealed the significance of the collagen network structural integrity to the aggregate mechanical response of the ACL and, hence, underlined the biomechanical factors that may help develop an engineering-based approach towards improving the therapeutic intervention for ACL pathologies.

*Address for correspondence: Malek Adouni, PhD, Physical Medicine and Rehabilitation Department, 710 North Lake Shore Drive, Chicago, IL 60611, USA.
Telephone number: +1 3122381000   Email: malek.adouni@northwestern.edu

Introduction

Within the knee joint, the anterior cruciate ligament (ACL) is one of the most frequently injured tissues, with an estimated incidence of ~ 75 cases per 100,000 people (Frobell *et al.*, 2007; Sanders *et al.*, 2016). Physically active adolescents and young adults are the most susceptible to contact and non-contact ACL injuries (Sanders *et al.*, 2016). However, the level of injury in older people is more serious, leading to complete rupture of the ligament and, thus, narrowing the treatment options to surgical reconstruction (Schilaty *et al.*, 2017). In addition, this injury leads to a protracted period of reduced activity, risk of other soft tissue injuries and, consequently, a higher socioeconomic burden (Myklebust and Bahr, 2005). Hence, many experimental studies have been conducted to help understanding the mechanism of the ACL injury and its associated effect on the kinematics and kinetics of the knee joint [(Bates *et al.*, 2018; Benos *et al.*, 2020; Blaker *et al.*, 2017; Homyk *et al.*, 2012; Kiapour *et al.* (2012) ACL injury mechanism is related to articular pressure distribution: a cadaveric and finite element (FE) investigation. In: Proceedings of the Summer Bioengineering Conference, pp 283-284, conference abstract; Levine *et al.*, 2012; Paschos *et al.*, 2010; Song *et al.*, 2004]. However, most of these investigations were limited to studying the load-mediated mechanism using mechanical ACL rupture or total/partial surgical ACL transection models. Driven by the concept of more closely mimicking the clinical conditions, the reproducibility and predictability of ACL and joint injury development studies are advantageous. However, the invasive nature of such approaches triggers inflammatory and adaptive responses in the joint and potentially confounds the biological response to injury (McLean *et al.*, 2015).

In addition to the load-mediated injury mechanism, cohort studies introduced additional factors to the matrix of reasons for ACL injuries, such as age, gender, neuromuscular factors and trauma (Ochi *et al.*, 2016). The effect of some of these intrinsic factors, studied by microscopy, has been described as an unbalanced process of tissue remodelling or activation of degraded enzymes by pro-inflammatory molecules (Blaker *et al.*, 2017; Georgiev *et al.*, 2018; Ireland, 2002; Ochi *et al.*, 2016; Riley, 2004; Slauterbeck and Hardy, 2001; Tang *et al.*, 2009c). Thus, the ACL injury may be described as a bottom-up process starting with depletion of proteoglycan and breakdown of collagen. This has later received significant attention from the molecular to the aggregate level either experimentally (Abrahams, 1967; Akizuki *et al.*, 1986; Catanese III *et al.*, 1999; Diamant *et al.*, 1972; Shen *et al.*, 2008; Shen *et al.*, 2011) or computationally using molecular dynamics simulations (Buehler, 2006; Chang *et al.*, 2012; Depalle *et al.*, 2016a; Liu *et al.*, 2014; Lorenzo and Caffarena, 2005; Nikolov and Raabe, 2008; Stevens, 2008; Tang *et al.*, 2010). A clear agreement has been reached on the significant influence of the molecular degradation mechanism upon the mechanical behaviour of the collagen fibril. However, to the authors' knowledge, most previous investigations were limited to the nano and micro levels, yet the extrapolation of the collagen micro-alteration to the tissue level response is still missing. Thereafter, exploring how molecular-level interactions combine to create a mechanical tissue response may play a potential role in understanding the mechanism of ACL injuries due to some intrinsic factors, hence improving the advancement of ACL damage or trauma treatments.

The purpose of the present study was to characterise the connection between tissue- and collagen-level mechanics in the ACL using a multiscale model. The developed computational construct took the ACL material behaviour at several structural hierarchies using a hierarchical multidomain coupling scheme linking the molecular dynamics to the FE simulations. The irreversible mechanical behaviour of the ACL was attributed to the inelastic behaviour of the tropocollagen molecules modelled using molecular dynamics simulations. Knowing the functional mechanisms associated with the relative contribution of one of the tissue key constituents, the collagen fibril network, may significantly improve ACL treatment strategies and, hence, the knee joint overall healthcare. The study hypothesis was that the integrity of the collagen network played a significant role in the expression of the ACL aggregate mechanical behaviour.

Materials and Methods

Collagen fibril coarse-grained model
The objective of the molecular dynamics simulations was to obtain stress-strain curves for collagen fibrils in ligaments with different volume and surface degradation coefficients for a fully crosslinked model. The methodology of the coarse-grained model (Fig. 1) was based on a mesoscopic model first developed by Buehler (2006).

The concept of the mesoscopic coarse-grained approach is based on reducing the number of simulated atoms by abbreviating the full molecular geometry (which consists of a triple-helical protein
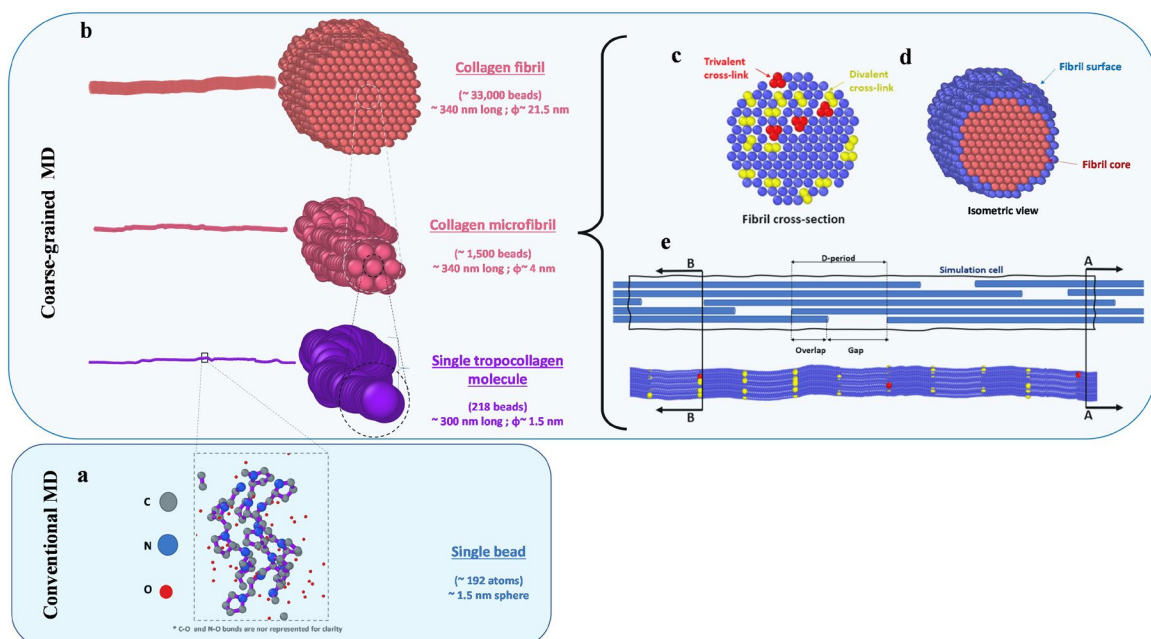

Fig. 1. Coarse-grained model of the collagen fibril. (**a**) 3D view of a single collagen bead. (**b**) The hierarchical structure of the collagen fibril coarse-grained model. (**c**) Trivalent-divalent crosslinks in the coarse-grained model. (**d**) The superficial and volumetric zones of the fibril that are subjected to degradation. (**e**) Cross-axial view of the simulated cell. Φ: diameter.

Table 1. Mesoscopic structural properties.

Molecular properties		Fibre properties	
Parameter	**Value**	**Parameter**	**Value**
Molecule number of atoms	3,134	Gap [nm]	40.0
Molecule total mass [g/mol]	287,000	Overlap [nm]	~ 28.2
Number of beads per molecules	218	D_period [nm]	~ 68.2
Mass of each bead [g/mol]	1,316	Length of fibril [nm]	341.0
Length along principal axis [nm]	30.11	Hexagonal lattice constant [nm]	1.652

Table 2. Pairwise and angle energy parameters.

Parameter	Value	Parameter	Value
ε: Lennard Jones [Kcal/mol]	6.87	θ_0: equilibrium bending angle [degree]	164-180
σ: Lennard Jones [nm]	1.472	K_θ: equilibrium bending constant [Kcal/mol/rad^2]	14.98

Table 3. Bond energy parameters.

Parameter	Molecule	Divalent	Trivalent
r_0: equilibrium distance [nm]	1.400	1.000	0.860
r_1: critical hyperplastic distance [nm]	1.820	1.200	1.220
r_b: bond breaking distance [nm]	2.100	1.468	1.489
k_{t0}: stretching strength constant [kcal/mol]	17.13	0.20	0.20
k_{t1}: stretching strength constant [kcal/mol]	97.66	41.84	54.60

structure of 3 chains of amino acids) into a single chain of beads or super atoms, where each bead represents several atoms (≈ 192 atoms in the present study) in the full atomistic model (Fig. 1**a**). By reducing the number of simulated atoms, collagen molecular simulations can access time and length scales impossible to reach when following the regular atomistic approach. This later requires from 50 million to a few billion atoms, which is unfortunately inaccessible using a simulation. In fact, a minimum of two orders of scale on the size of the fibril or the strain rate used can be gained. The collagen molecule has a diameter of 1.65 nm and a length of 301 nm [Protein Data Bank entry 3HR2; X-ray crystallography (Orgel *et al.*, 2006)]. This concept is detailed in previous publications (Buehler, 2006; Depalle *et al.*, 2015; Depalle *et al.*, 2016b) (Fig. 1**b**-**e**).

In the present model, tropocollagen molecules of 218 beads (Depalle *et al.*, 2015) were used, where the coordinates were obtained by averaging the geometric position of adjacent atoms from experimental measures. The resulting structure was a chain of nearly equally distributed beads oriented in the equilibrium state, with angles varying from 164° to 180°. Table 1 presents details on the mesoscopic model parameters (molecular).

The collagen fibril was built by reproducing the created molecule orthogonally to its principal axis. Using X-ray diffraction, Fang and Holl (2013) showed that the molecules are packed in a quasi-hexagonal array where each group of 5 molecules packs together to form a microfibril. Within the microfibril, molecules exhibit 5 gap/overlap regions along the fibril's length, with a periodic length consisting of one gap and one overlap region. The periodic length (D_period) ranges from 61 nm to 75 nm (Sweeney *et al.*, 2008). The gap to D_period ratio ranges from 0.54 (Gautieri *et al.*, 2011; Sweeney *et al.*, 2008) to 0.60 (Watanabe-Nakayama *et al.*, 2016). In the present work, it was assumed that the molecules were arranged hexagonally under a constant lattice of 1.652 nm, gap length of 36 nm and overlap length of 28.2 nm, which generated a structure of 32,918 beads (151 molecules) (Fig. 1**b**-**e**).

After building the fibril geometry, enzymatic crosslinks were added to the model. Unlike non-enzymatic crosslinks, or advanced glycation end-products, enzymatic crosslinks are protein-protein bonds that are well understood and modelled in previous works. Enzymatic crosslinks connect telopeptide and helical residues generating a divalent (immature) crosslink between the nearest neighbour of adjacent molecules. A possible further reaction of the divalent crosslink may lead to a trivalent one (mature), linking 3 molecules to 2 adjacent molecules (nearest neighbours). A ratio of 33 % of trivalent crosslinks to the total number of crosslinks was used during this investigation (Saito *et al.*, 1997). Both enzymatic and non-enzymatic crosslinks appear to correlate with several conditions such as skin and bone disorders, diabetes and Alzheimer's disease (Gautieri *et al.*, 2014; Snedeker and Gautieri, 2014; Takeuchi *et al.*, 2004; Vasan *et al.*, 1996). In addition, hyperelastic behaviour was considered for both divalent and trivalent crosslinks (Table 2).

The present study used a fully crosslinked collagen fibril model where all molecule ends were linked to one adjacent bead (divalent crosslink) or two adjacent beads (trivalent crosslink). To simulate degradation in

the collagen fibril, beads were cleaved from the model based on an algorithm simulating the cumulative effect of matrix metalloproteinase (MMP)-driven degradation (Connolly, 1983; Perumal *et al.*, 2008; Powell *et al.*, 2015). Two types of degradations were considered in the present study.

1. Volume degradation. The beads were randomly removed from all over the sample regardless of their position. All interactions involving those beads were also removed. The volume degradation coefficient δ_V was defined as the ratio between the number of removed beads and the total number of beads.

$$\delta_V = \frac{n_{removed}}{n_{total}}$$

2. Surface degradation. The beads were only removed from the surface (Fig. 1**d**). A surface bead was defined as a bead with a coordination number of less than 12 (bulk coordination number). Beads on the surface had coordination numbers of 10, 8, 6 or 4. The ratio of surface elements to the total number of elements varied drastically depending on the diameter of the simulated fibril. For the model described in the present study, 9,156 of the 32,918 beads were on the surface ($\approx$ 27 %). For a larger fibril with a diameter of 100 nm, only 6 % of the beads were on the surface. Therefore, it was more meaningful to define the surface degradation coefficient δ_S as the ratio between the number of removed beads and the number of surface beads.

$$\delta_S = \frac{n_{removed}}{n_{surface}}$$

δ_S and δ_V are related according to

$$\delta_S = \delta_V \, \frac{n_{total}}{n_{surface}}$$

The mechanical properties of the collagen fibrils resulted from the force field governing the beads. The formulation of this force field was implemented in several studies (Buehler, 2008; Depalle *et al.*, 2015; Depalle *et al.*, 2016a) and was proven to be accurate in reproducing the actual behaviour of the fibril in molecular dynamics (MD) simulations. The potential field adopted was governed by three main forces.

$$E = E_{inter} + E_{bond} + E_{angle}$$

E_{intern} is a Lennard-Jones pairwise interatomic potential linking beads from adjacent molecules in the radial direction. The Lennard-Jones potential is given by:

$$E_{inter} = 4\varepsilon \left(\left(\frac{\sigma}{r}\right)^{12} - \left(\frac{\sigma}{r}\right)^{6} \right)$$

where ε and σ represent the minimum energy and the characteristic distance of the Lennard-Jones potential, respectively. Table 2 shows parameters for pairwise potential. E_{bond} is hyper-elastic bond energy linking every two adjacent beads from the same molecule. It is represented by 3-regimes potential energy given by

$$F_{bond} = \frac{\partial E_{bond}}{\partial r} = \begin{cases} K_{T0}(r - r_0) & , r < r_1 \\ K_{T1}(r - \overline{r_1}) & , r_1 < r < r_b \\ 0 & , r > r_b \end{cases}$$

where K_{T0} and K_{T1} are spring constants, r_1 is the distance at which the hyper-elastic behaviour of the bond is triggered, r_b is the bond-breaking distance and
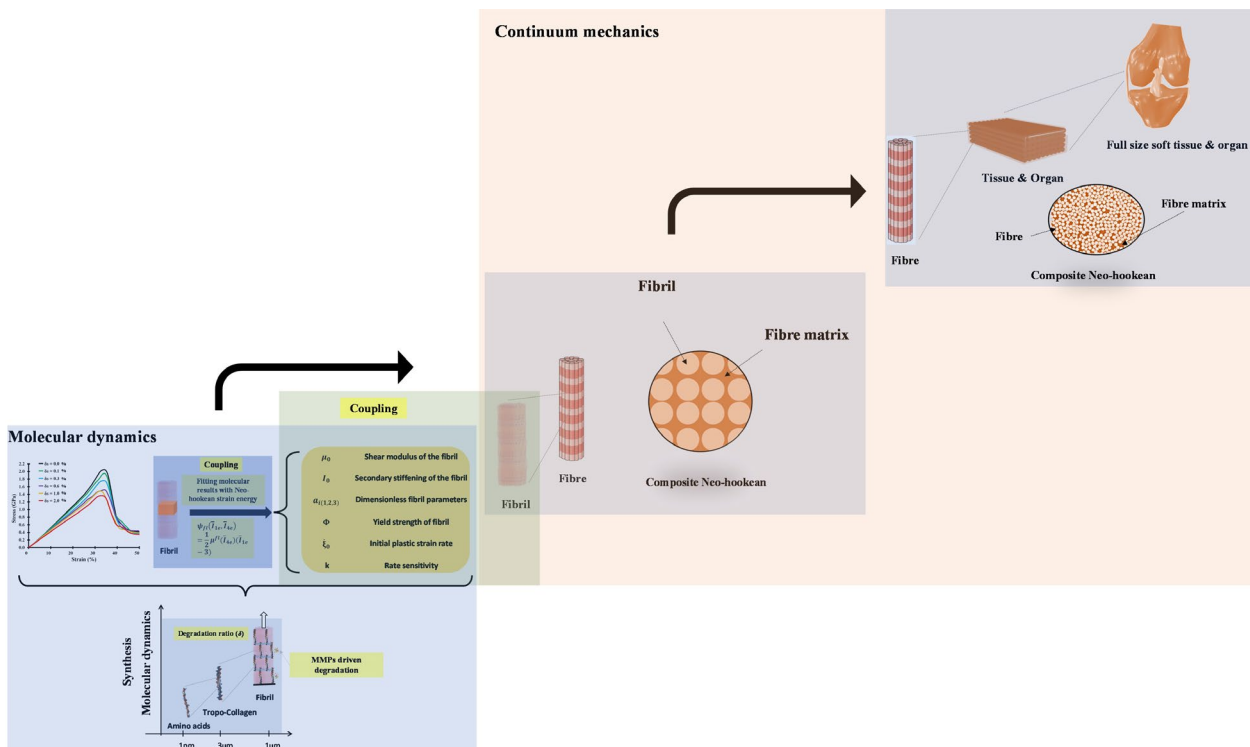

Fig. 2. Hierarchical diagram showing the structural characteristics of the two different syntheses (molecular dynamics and continuum mechanics) of the ACL model as well as the coupling between them.

$\overline{r_1}$ is the continuity of the force-field constant. Table 3 shows parameters for the bond energy. E_{angle} is a harmonic 3-body interaction angular energy between each 3 adjacent super atoms from the same molecule. The purpose of this energy is to control the bending angle between the beads.

$$E_{angle} = K_\Theta (\theta - \theta_0)^2$$

where K_θ denotes the bending strength, θ the actual angle between each 3 consecutive beads and θ_0 the equilibrium angle (Table 2).

The geometric model was created using MatlabR2021A (The MathWorks, Natick, MA, USA) by averaging the positions of the tropocollagen molecule atoms and replicating the chain of beads in the radial directions. All molecular simulations were performed using LAMMPS molecular dynamics software (Plimpton, 1995) (Sandia National Laboratories, Albuquerque, NM, USA). A 10 fs time step was used. The fibril was relaxed at constant pressure/temperature for 1 ns, then at constant volume/temperature to release the residual stress for an additional 1 ns. The tensile deformation of the fibril was modelled using an axial velocity constraint applied on both ends of the fibril associated with a longitudinal periodic boundary condition to relieve any surface energy effects. Then, virial stresses and the fibril volume were used to determine the stress-strain behaviour. Finally, the OVITO package (Stukowski, 2009) [Lawrence Livermore National Laboratory (LLNL), CA, USA] was employed for the visualisation of the results.

Fibril hyperelastic model

In this multiscale structure, a homogenised continuum representation of the soft tissue was employed (Fig. 2). Each continuum material point reflects the tissue's statistically homogenous representative volume element (RVE) response defined by the volume average of the deformation gradient over the RVE (Tang *et al.*, 2009a). Thus, the total deformation gradient tensor was decomposed in a sequence of elastic (*e*) and plastic (*p*) elementary deformation

$$\overline{F} = \overline{F}_e \overline{F}_p$$

(Asaro and Rice, 1977; Lee, 1969). The developed invariants from these tensors are

$$\overline{I}_1 = \mathbf{tr}\,(\overline{C} = \overline{F}\,\overline{F}^{\mathrm{T}})$$

and

$$\overline{I}_4 = n_0\,\overline{C}\,n_0^t,\ \overline{I}_{1f} = \overline{I}_4 + 2\overline{I}_4^{-\frac{1}{2}}$$

where n_0 is the reference direction of the fibril in the initial configuration. After that, the fibril model was developed based on a modified formulation of generalised Neo-Hookean material, where the following equation defines the expression of the strain energy function

$$\begin{cases} \psi_{fb}(\overline{I}_{1e}, \overline{I}_{4e}) = \frac{1}{2}\mu^{fb}(\overline{I}_{4e})(\overline{I}_{1e} - 3) \\ \mu^{fb}(\overline{I}_{4e}) = \mu_0 \left(tanh\left(a_1(\overline{I}_{4e} - 1)\right) + a_2 exp\left(a_3(\overline{I}_{4e} - I_0)\right) \right) \end{cases}$$

I_0, a_i and μ_0 represent the secondary stiffening, dimensionless parameters and the shear modulus
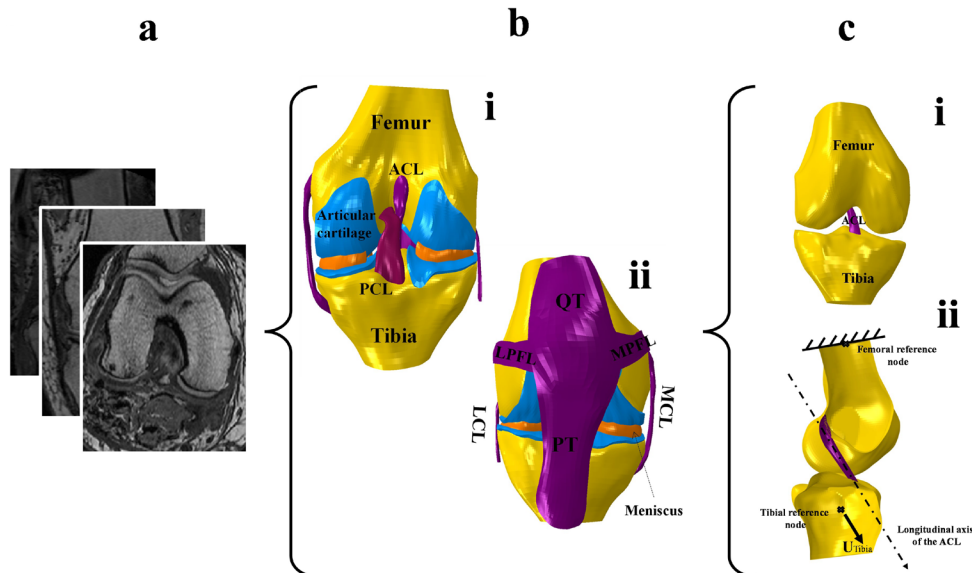

Fig. 3. Knee finite elements model. (**a**) MR-images of the knee joint. (**b**) Anterior (i) and posterior (ii) views of the 3D FE model of the knee show the corresponding soft tissues and articular surfaces acting on the bones. ACL, posterior cruciate ligaments (PCL), medial and lateral collateral ligament (MCL, LCL), lateral patellofemoral (LPFL), medial patellofemoral (MPFL), quadriceps tendon (QT) and patellar tendon (PT) cartilage layers as well as menisci are shown. (**c**) ACL FE model (i) with the boundary conditions (ii) employed to mimic the tensile test (bones were considered to be a rigid body). More details on the system of axes and the joint centre calculations can be found in Erdemir (2016).

of the fibril, respectively. The introduced hyperbolic modification of the formulation of the fibril strain energy was based on the observed stiffness evolution of the fibril rooted in the wrinkled fibres (Buehler and Ballarini, 2013). Low load sustainability initially characterised the fibril stiffness evolution, followed by a stiff elastic regime controlled by the enzymatical crosslinks between the tropocollagen molecules (Buehler, 2008). Then, the effective stress ($\sum_{eff}$) of the fibril was connected to the Mandel stress (M) as follow.

$$\begin{cases} \Sigma_{eff} = M : dev(n_0 \otimes n_0) \\ M = F^{eT} \overline{\sigma} F^{e-T} = F^{eT} \left(2I_{4e} \frac{\partial \psi_{fb}}{\partial I_{4e}} n_e \otimes n_e \right) F^{e-T} \end{cases}$$

where $\overline{\sigma}$ and $n_e = \frac{F_e n_0}{\sqrt{I_{4e}}}$ stand for the macroscopic Kirchhoff stress and the current fibril direction, respectively. By simple mathematical manipulation, effective stress follows the equation

$$\Sigma_{eff} = \frac{4}{3} I_{4e} \frac{\partial \psi_{fl}}{\partial I_{4e}}$$
.

The evolution of the fibril plastic deformation is driven by the following equations: (a) flow resistance, (b) single-crystal strain rate, (c) Karush-Kuhn-Tucker loading/unloading conditions (Belytschko *et al.*, 2014; Gasser and Holzapfel, 2002; Tang *et al.*, 2009a)

$$\begin{cases} \dot{\xi} = \dot{\xi}_0 \left| \frac{\Sigma_{eff}}{\phi} \right|^{\frac{1}{k}} sig(\Sigma_{eff}) & (a) \\ \dot{\Phi} = h\dot{\xi} \left(1 - \frac{\Phi}{\Phi_s} \right) & (b) \\ \dot{\xi} \geq 0; \ f = (\Sigma_{eff} - \Phi) \leq 0; \ f\dot{\xi} = 0 & (c) \end{cases}$$

where ξ_0 is the initial plastic strain rate; Φ the yield strength of fibril; h, k and Φ_s the softening or hardening rate, rate sensitivity and saturated flow str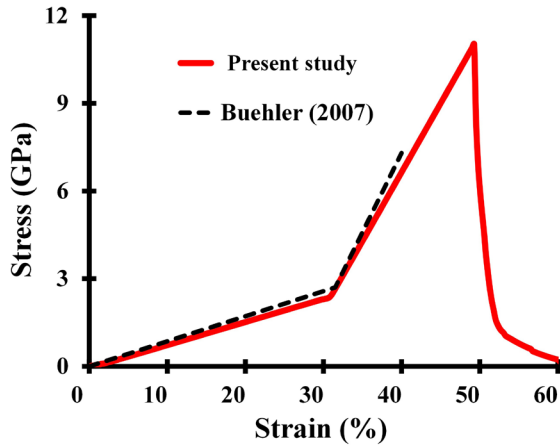ength of the fibril, respectively. Owing to fibril softening related to the breakage of crosslinks, the saturated flow strength, Φ_s, is generally chosen to be smaller than the initial yield strength of the fibril (Φ_0) (Tang *et al.*, 2009a). This is a function of the degradation ratio (δ) and was defined in the present study by the density function derived from the mesoscopic model (Fig. 1). After the calculation of the plastic strain rate, the plastic and the elastic deformation tensors were integrated using the plastic velocity gradient formula.

$$\begin{cases} F_p = \int \left(\dot{\xi} \, dev(n_0 \otimes n_0) F_p \right) \\ F_e = F \, F_P^{-1} \end{cases}$$

The plastic deformations gradient is unity

$$(F_p = I \text{ and } F_e = F)$$

up to the yield point and only starts interfering after the yield of the fibril. Thus, the plastic deformation initiation is solved using the equality equation between the effective stress and the yield strength of the fibril. This later was determined from the molecular dynamics results.

Connective tissue model
As a continuation of the hierarchical hyper-elastoplastic model, the above fibril reinforced an incompressible Neo-Hookean matrix to model the
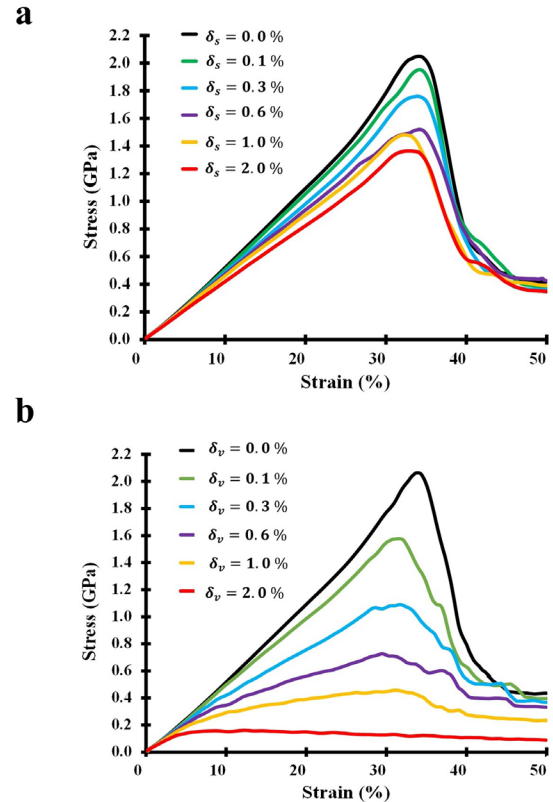
Fig. 4. Predicted stress-strain changes in the single tropocollagen molecule along with Buehler *et al.* (2008) model predication.

Fig. 5. Fibril strain-stress behaviour. Strain-stress behaviour of the collagen fibril as a function of (**a**) surface (δ_s) and (**b**) volumetric (δ_V) degradation rate predicted using the coarse-grained model under axial tensile testing.

fibre structure (Fig. 2). The fibre total elastic strain energy density is the summation of the elastic strain energies under extension (*t*) and shear (*s*)

$$\psi_{fi}(\bar{I}_{1fb}, \bar{I}_4, \bar{I}_{4e}) = \left[v_{fb}\psi_{fb}(\bar{I}_{1e}, \bar{I}_{4e}) + v_m\left(\frac{\mu_{fm}}{2}(\bar{I}_{1f} - 3)\right)\right]_t$$
$$+ \left[\frac{1}{2}\mu_{fm}\frac{(1+v_{fb})\mu^{fb}(\bar{I}_{4e}) + \mu_0(1-v_{fb})}{(1-v_{fb})\mu^{fb}(\bar{I}_{4e}) + \mu_0(1+v_{fb})}(\bar{I}_{1fb} - \bar{I}_{1f})\right]_s$$

where μ_{fm}, v_{mb} and v_{fb} are the shear moduli of the fibre matrix, the volume fraction of the fibre matrix and the fibrils, respectively. The shear part characterises the junction interaction between the fibril and the matrix (DeBotton *et al.*, 2006; Guo *et al.*, 2008; Guo *et al.*, 2006). Using the same mixed formula, the total strain energies of the soft tissue in which the collagen fibre reinforced the composite material are given by:

$$\psi_t(\bar{I}_{1fb}, \bar{I}_4, \bar{I}_{4e}) = \left[v_f\psi_{fi}(\bar{I}_{1fb}, \bar{I}_4, \bar{I}_{4e}) + v_m(\frac{\mu_m}{2}(\bar{I}_1 - 3))\right]_t$$
$$+ \left[\frac{1}{2}\mu_m\frac{(1+v_f)\mu^{efffb}(\bar{I}_{4e}) + \mu_m(1-v_f)}{(1-v_f)\mu^{efffb}(\bar{I}_{4e}) + \mu_m(1+v_f)}(\bar{I}_1 - \bar{I}_{1fb})\right]_s + \psi_{vol}(\bar{J})$$

where μ_m, v_m and v_f are shear moduli of the tissue matrix, the volume fraction of the tissue matrix and the fibre,respectively, and

$$\mu^{efffb}(\bar{I}_{4e})$$

is the effective shear modulus of the fibril-fibre matrix and is given by

$$\mu^{efffb}(\bar{I}_{4e}) = \mu_{fm}\frac{(1+v_{fb})\mu^{fb}(\bar{I}_{4e}) + \mu_0(1-v_{fb})}{(1-v_{fb})\mu^{fb}(\bar{I}_{4e}) + \mu_0(1+v_{fb})}.$$

The strain-energy function of the tissue can be further expressed by

$$\psi_t(\bar{I}_1, \bar{I}_{1f}, \bar{I}_4, \bar{I}_{4e}) = \frac{1}{2}(v_f v_{ml}\mu_{fm} + v_m\mu_m)\left(\bar{I}_4 + \frac{2}{\sqrt{\bar{I}_4}} - 3\right) + \frac{1}{2}(v_f v_{fl}\mu_{fl})\left(\bar{I}_{4e} + \frac{2}{\sqrt{\bar{I}_{4e}}} - 3\right)$$
$$+ \frac{1}{2}\mu^{eff}\left(\bar{I}_1 - \bar{I}_1(F_f)\right) + \frac{E_K}{2}(\bar{J}-1)^2.$$

At the macroscopic continuum level, the Clausius-Duhem dissipation inequality and the incompressibility constraint of the soft tissue are expressed by

$$\begin{cases} \overline{\sigma}:\overline{D} - \dot{\psi}_t \geq 0 \\ \dot{\bar{J}} = J\overline{C}^{-1}:\dot{\overline{C}} = 0 \end{cases}$$

where $\overline{\sigma}$ is the macroscopic Kirchhoff stress of the continuum tissue, $\overline{D}$ is the macroscopic rate of deformation and $\bar{J} = \det(\overline{C})$. By satisfying the inequality and the constraint condition, the total Cauchy stress $\sum_t$ can be expressed with fibrillar $\sum_f$ and nonfibrillar $\sum_{nf}$ stress tensors as

$$\begin{cases} \Sigma_t = \Sigma_{nf} + \Sigma_f \\ \Sigma_{nf} = \frac{2}{J}\left(\bar{I}_1\frac{\partial\psi_t}{\partial\bar{I}_1}dev(\overline{B}) + (E_K\bar{J}(\bar{J}-1))I\right) \\ \Sigma_f = \frac{2}{J}\left(\bar{I}_4\frac{\partial\psi_t}{\partial\bar{I}_4}dev(n\otimes n) + \bar{I}_{4e}\frac{\partial\psi_t}{\partial\bar{I}_{4e}}dev(n_e\otimes n_e)\right) \quad if\ \bar{I}_4 > 1 \\ \Sigma_f = 0 \quad if\ \bar{I}_4 \leq 1 \end{cases}$$

The numerical performance of the developed materials model and its basic features were successfully tested with single and multiple elements. Tang *et al.* (2009b) and Adouni *et al.* (2021) have explained in details the constitutive model used in the present study. Then, this model was assigned to the ACL structure.

Molecular dynamic-softening hyper-elasticity approach

4 parameters of the developed model ($\mu_m, \mu_{fm}, v_f, v_{fl}$) were chosen based on a prior calibration process using a statistical approach (Adouni *et al.*, 2021). The rest of the parameters that are driving the fibrils response

$$\mathbf{x} = (\ \mu_0,\ I_0, a_{i(1,2,3)}, \Phi, \dot{\xi}_0, k\ )$$

were next calculated by fitting them to the predicted results of molecular dynamics simulation (MDS). The fitting procedures, which represented coupling between the molecular and continuum syntheses (Fig. 2), were performed *via* non-linear optimisation using the lsqnonlin function available in MatlabR2021A. During the optimisation process, the hierarchal model was called to simulate one element tensile test (50 % axial strain). Then, the FE- and MD-computed fibril stresses were assigned into MatlabR2021A (least square algorithm) to minimise the objective function *f(x)*.

$$f(x) = \frac{\sigma_{fl}^{FE}(x) - \sigma_{fl}^{MDS}}{\sigma_{fl}^{MDS}}$$

where $\sigma_{fl}^{FE}(x)$ is the axial stress of the fibril predicted by means of the hyper-elastoplastic model as a function of the unknown fibril materials parameters

and $(x), \sigma_{fl}^{MDS}$ is the axial stress of the fibril predicted by MDS under the fibril superficial and volumetric degradation. An iterative algorithm based on the Latin hypercube sampling function (*lhs*) was used to identify the initial input for the optimisation procedure. To ensure an unbiased estimate of the fibril parameters, additional verification was conducted using the globalserch solver (*gs*).

ACL model

A female 70 years old subject, 170 cm tall and weighing 77 kg was used to generate the geometry of the knee model (Open Knee Public Domain Repository at Simtk.org) (Erdemir, 2016). The knee was placed in full extension and the scanning process employed a 3D spoiled gradient-echo sequence with fat suppression, repetition time = 30 ms, time to echo = 6.7 ms, flip angle = 200 °, field of view = 150 mm × 150 mm, slice thickness = 1.5 mm. The imaging was conducted in 3 anatomical planes (axial, sagittal and coronal) using a 1.0 Tesla extremity magnetic resonance imaging (MRI) scanner at the Biomechanics laboratory of the Cleveland Clinic (Cleveland, OH, USA). These images are optimal for differentiating between muscles, tendons, tissue fascia and bone (Erdemir, 2016) (additional details about the scanning protocol can be found in Open Knee Public Domain Repository, Web ref. 1). Then, the image data set was imported into an MRI viewing and segmentation analysis package (3D slicser4.8) and re-sampled in the sagittal, coronal and axial planes (Fig. 3**a**). The muscle-bone junctions were identified from the MRI images following the

Table 4. Material parameters of the fibril found through the data fitting procedure.

	Parameters	Lower bound	Upper bound	Surface degradation parametric values (SD)	Volume degradation parametric values (SD)
μ_0	Shear modulus of the fibril (MPa)	1,250	4,250	3,489,292 (99,996)	3,116,623 (405,448)
I_0	Secondary stiffening of the fibril (unitless)	1.5	2.9	2.568 (0.110)	2.498 (0.164)
a_1	Dimensionless fibril parameter 1	0.05	2	1.893 (0.060)	1.809 (0.147)
a_2	Dimensionless fibril parameter 2	250	1,000	814,144 (31,817)	787,997 (43,365)
a_3	Dimensionless fibril parameter 3	20	110	72,499 (10,556)	57,499 (17,791)
Φ	Yield strength of fibril (MPa)	411	2,500	1,646,728 (248,775)	1,302,833 (495,562)
ξ_0	Initial plastic strain rate (s^{-1})	0.01	0.025	0.021 (0.003)	0.017 (0.0021)
k	Rate sensitivity (unitless)	0.04	0.09	0.050 (0.0015)	0.056 (0.0065)

procedure outlined by Dhaher and Kahn (2002). Polygonal surfaces were used to generate a FE mesh of the knee joint using the Hypermesh pre-processor (Altair Engineering, Troy, MI, USA). The structure of the tibiofemoral joint was adjusted to match the dimension given in the open knee public domain repository at Simtk.org (Web ref. 1) (Erdemir, 2016). Bones were defined as rigid bodies (Donahue *et al.*, 2002) using 4-node quadrilateral elements that injunction with elastic boundaries with the articular cartilages. 8-node hexahedral elements were used to represent the articular cartilages, ligaments and menisci (Fig. 3**b**). From the above model, only the ACL with its junction bones (femur and tibia) were considered during the FE simulation (Fig. 3**c**). The ligament meshed with respect to 6 % sensitivity analysis (difference in the axial stress) employing reduced integration of 8-node hexahedral elements with an average side length of 0.38 mm (Abaqus 6.14). Finally, each hexahedral element at the integration point was characterised by a local system axis through ligament structure to accurately incorporate the collagen networks' orientation.

The above ACL model was simulated at full extension under axial tension by fixing the femoral bone and pulling the tibial bone by an axial strain of 17 % parallel to the average direction of the collagen fibres (longitudinal axis of the ACL) (Fig. 3**c**, ii). These additional simulations were carried out to examine the effect of the molecular fibril surface and volume degradation mechanism on the aggregate mechanics of the ACL. Abaqus explicit was used during all simulations with a short step time of 0.01 s to mimic quasi-static analysis. Computations were performed using an Intel® Core™ i7-7700 CPU 3.60 GHz dual processor, 32.0 GB of RAM, HP EliteDesk machine.

Results

The stress-strain behaviour of one tropocollagen molecule is depicted in Fig. 4. 3 different regimes

characterised this behaviour, which were explained by 3 different mechanisms. First, on the presented curve, a hardly visible regime with low stress was due to a change in the angle energy. Second, the first linear regime with an elastic modulus of ~ 7.9 GPa was mainly due to the bond stretching below the hyper-elastic critical distance r_1. Third, the second linear regime was characterised by a sharp change in the stiffness (elastic modulus of ~ 47.1 GPa), as the bond distance reached the hyper-elastic critical distance r_1. Finally, the molecule broke when interatomic distances reached the breaking distance.

Fig. 5 depicts the obtained stress-strain curve for the collagen fibril for different surface and volume degradations. Qualitatively, the overall trend of both curves was intuitive: increasing degradation amount decreased both the tensile strength and the tensile strain of the fibril. Fig. 5**a** shows the effect of surface degradation on the overall properties of the fibril. The trend of the curves showed that with increased values of δ_S, the overall properties of the fibril deteriorated. The differential effect of δ_S decreased for more degraded fibrils. For example, at $\delta_S = 0.1$ %, a 9 % decrease in tensile strength was observed, for $\delta_S = 0.6$ % (0.5 % additional degradation) an additional degradation of 26 % was observed. The effect of the surface degradation was limited to the surface beads, maintaining the effect of the core of the fibril intact. At $\delta_S = 2$ %, a 35 % reduction in the strength of the fibril was observed. Further increasing the surface degradation did barely change its properties, while a more devastating effect on the stress-strain behaviour of the fibril was observed with volume degradation (Fig. 5**b**). For example, at $\delta_V = 0.6$ %, a 71 % decrease in fibril strength was observed. This was because, for lower values of δ_V, beads were mostly removed from different molecules, thus disabling their stretching capability. The effect of the degradation continued until all molecules were compromised.

Nonlinear curve fitting was employed to determine the fibril material parameters by considering the kinematics of native and degraded collagen given by

MD simulation. Acceptable fits to MDS fibril results were observed for both degradation processes, with a coefficient of determination R^2 equal to 0.961 ± 0.02 and 0.924 ± 0.04 for the surface and volume degradations, respectively. Table 4 summarises the input parameters' mean and standard deviation (SD) values for the considered degradation processes, where the SD represented the dispersion of the parametric values. Fig. 6 shows the maximum stress-strain variation in the aggregate mechanics of the ligament for the degraded fibrils along the collagen axial direction. A differential behaviour was observed for both simulated degradation mechanisms (δ_S and δ_V). In addition, both degradation mechanisms were characterised by a clear effect on the elasticity of the ACL. For example, a 0.6 % surface and volume degradation decreased the ACL elastic axial stress by around 25 % and 30 %, respectively, compared to the native fibril at the toe region (0 to 2.5 % axial strain). Furthermore, the decrease in the ACL stiffness aggravated in the linear and yielding regions, reaching its maximum of ~ 63 % diminution in yielding stress with 0.6 % fibril volume degradation (Fig. 6). The yielding strain varied between 11.5 and 12.6 % for the surface degradation and 9 and 12.6 % for the volume degradation (Fig. 6,7).

Under 10 % axial pre-yielding strain, nonuniform distributions have been observed in all stages of the collagen surface degradations (Fig. 8). In addition,
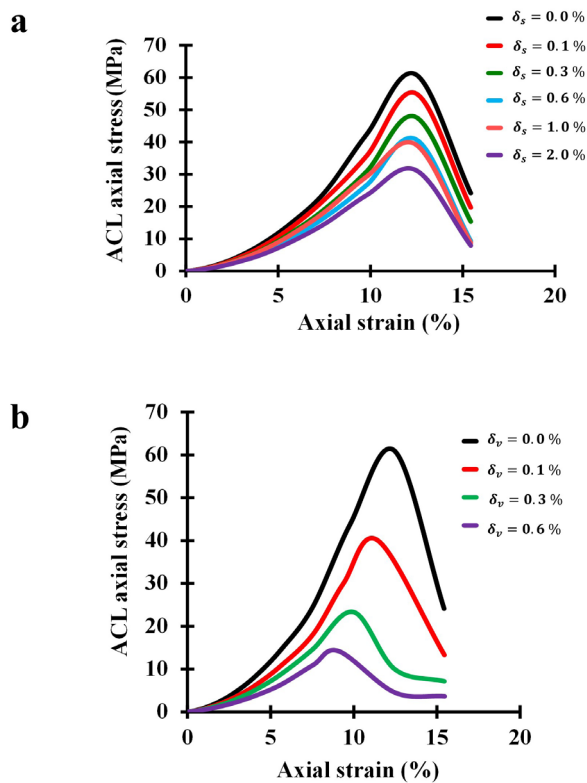
almost the same trends of stress distribution were computed with volume degradation at 7.5 % applied elastic strain (Fig. 9). Both degradation mechanisms led to a stress concentration at the posterolateral side near the tibial junction (Fig. 8,10). The choice of lower elastic strain with volume degradation scenario was considered to limit the above comparison to the elastic zone. Spatial distribution of the plastic elongation (failure indicator) was limited in most simulated cases to the collagen fibre of the superficial layer of the ACL (2 layers of hex elements) (Fig. 9,11). The degradation moved a bit deeper under the concentrated area of elongation in the advanced volume degradation. The area of the damage increased significantly with the increase in the rate of the molecular damage, reaching its maximum covering at 0.6 % fibril volume degradation (Fig. 11). This large area of ACL damage was associated with a maximum plastic elongation of 36 % located at the highest stress element.

Discussion

The present work aimed to define the theoretical relationship between tissue- and collagen-level mechanics in the ACL. Therefore, a multiscale frame connecting a molecular coarse-grained to fibril reinforced hyper-elastoplastic model was analysed. This engineering frame considered the soft tissue's structural architecture, starting from the collagen
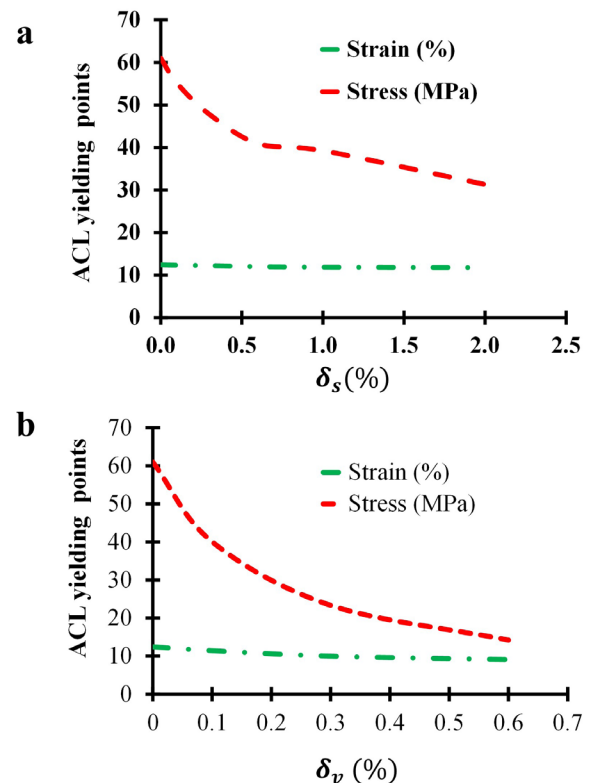

Fig. 6. ACL strain-stress behaviour. (**a**) ACL FE model with the boundary conditions employed to mimic the tensile test. (**b**) Stress-strain behaviour of the ACL as a function of (**a**) surface (δ_S) and (**b**) volumetric (δ_V) degradation.

Fig. 7. ACL yielding behaviour. Computed ACL yield strength (red) and strain (green) as a function of (**a**) surface (δ_S) and (**b**) volumetric (δ_V) degradation.

molecule that form fibrils to whole soft tissue. Unbalanced collagen due to mediated degradation by MMPs drove the damage mechanism. Results indicated a difference in the mechanical response between fibril and ACL when the tissue was subjected to an axial load. The main difference was expressed at yield reaction, where a much greater ability of damage support was observed in the scale of the fibril level compared with tissue level. Furthermore, independent of the degradation mechanism of the fibril, the capacity of the ACL to support the tensile load without failure was reduced significantly. The findings shed light on the importance of the collagen network and the changes in its mechanics caused by the unbalanced fibril level, which impacts aggregate tissue behaviour.

At the molecular level and during the tensile stress test, the angles on the fibril are first straightened since the angle energy is much smaller than both bond and pairwise energies. Then, with increasing strain, the internal stress starts to build up in the fibril until the pairwise forces can no longer resist the shear forces induced between the molecules. Then, the molecules start sliding and stress decreases (generally known as the low strain regime). When crosslinks are present in the fibril, they provide additional resistance to the shearing between molecules and, therefore, retard the sliding threshold, increasing the ultimate tensile strain and stress (generally known as the high strain regime) (Buehler, 2006; Depalle *et al.*, 2015). Herewith native fibril (fully crosslinked and non-degraded), the present computed tangent
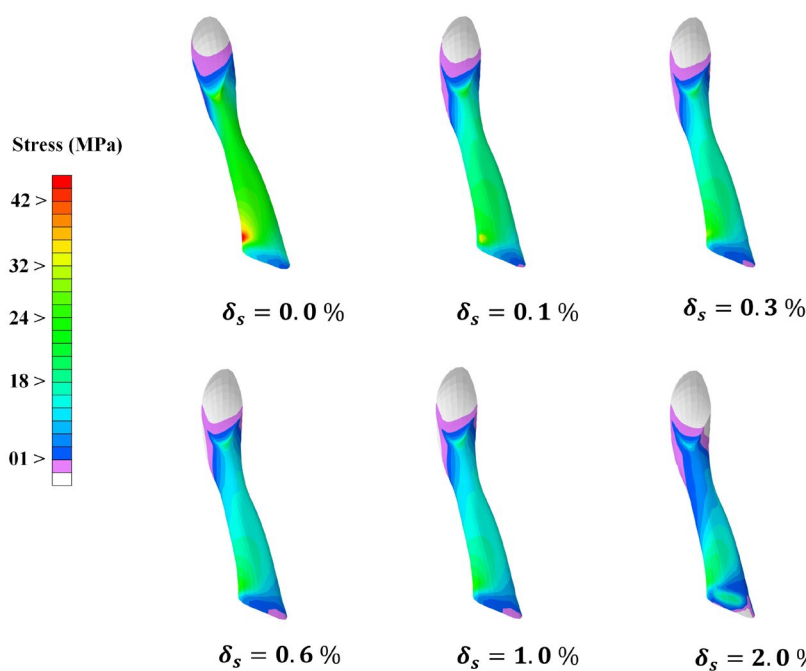

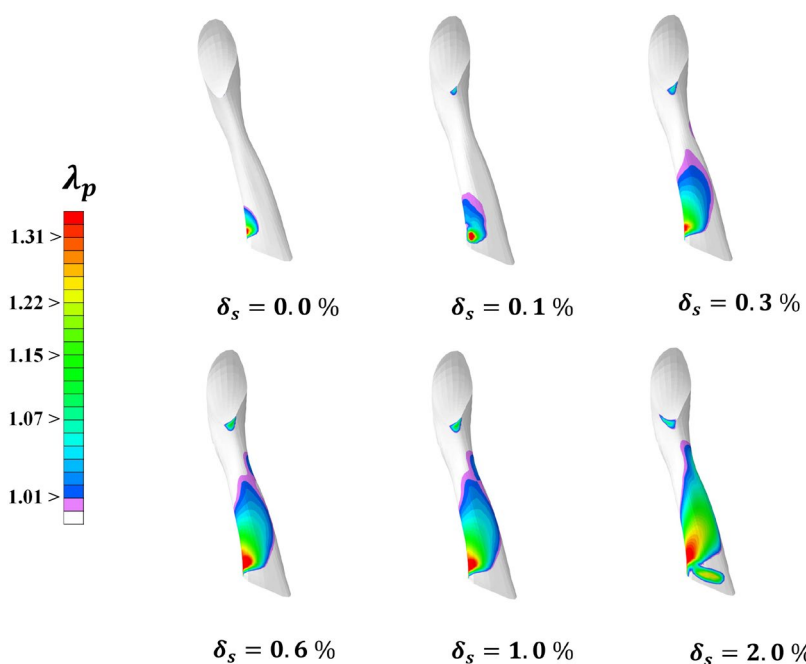**Fig. 8. Computed stress distribution in the ACL at 10 % axial strain (elastic zone) as a function of surface (δ_s) degradation.**

Fig. 9. Computed ACL damage distribution (plastic change) at 3 % post-yielding strain as a function of surface (δ_s) degradation.

Table 5. Comparison of obtained mechanical properties with no fibril degradation (δ = 0 %).

	Type of crosslinks	Young modulus	Ultimate tensile strength	Ultimate tensile strain
Depalle *et al.* (2015)	Divalent	4.18 GPa	1.42 GPa	32 %
Malaspina *et al.* (2017)	33 % trivalent	3.58 GPa	1.44 GPa	32 %
Present study	Divalent	4.88 GPa	1.70 GPa	30 %
	33 % trivalent	4.78 GPa	2.02 GPa	35 %

Table 6. Material properties of human and animal ACL [mean (SD)] *versus* FE predictions.

Specimen type	Ultimate strain (%)		Tensile strength (MPa)		Tangent modulus (MPa)	
	Published measurements	Present investigation	Published measurements	Present investigation	Published measurements	Present investigation
Human ACL (Butler *et al.*, 1986)	15 (1.8)	12.575	39.4 (6.5)	58.94	345 (22.4)	388.16
Canine ACL (Kwan and Woo, 1989)	16.0 (2.5)	-	56.0 (6)	-	476 (87)	-
Human ACL (Noyes *et al.*, 1974)	18 (5.3)	-	48.9 (7.2)	-	418 (119)	-
Human ACL (Tohyama and Yasuda, 2011)	14.1 (1.7)	-	68.2 (11.8)	-	332 (58.3)	-

modulus at low and high strain levels were about 4.7 GPa and 8.8 GPa, respectively. These predicted results were in good agreement with the measured ones using an atomic force microscope, where the values varied from 5 to 11.5 GPa (Wenger *et al.*, 2007). Thus, numerically and within an acceptable range of difference, the proposed model could reproduce the fibril mechanical behaviour predicted by Depalle *et al.* (2015) and Malaspina *et al.* (2017) under normal and degraded cases (Fig. 12**a**,**b** and Table 5). These small differences could be attributed to several reasons, such as the considered number of beads per molecule, the random factor used to drive the degradation mechanism and the difference in the gap/D $_{period}$ ratio. Even with the clear consistency in the predicted elasticity of a single tropocollagen molecule (Fig. 4), a lower estimation of the stress-strain behaviour of the fibril was predicted using the present model when it was compared with the two-dimensional collagen fibril mesoscale model (Buehler, 2008; Tang *et al.*, 2010). The discrepancy between models may be explained by a combination of size effects, entropic effects and model parameterisation errors.

The degradation of the surface of the fibril mainly affected the elastic moduli of the second regime (high strain), decreased failure stress and decreased toughness. Moreover, the simulated results indicated a significant alteration to the mechanical behaviour of the fibril caused by a small percentage of surface degradation ($\delta_s = 0.1$ %). However, as the degradation progressed beyond 2.0 %, these changes became insignificant. Therefore, the cross plot between the failure stress and percentage of surface degradation was expressed as a survivorship curve, with a rapid decay at minimal degradation rate and a plateau type of behaviour at higher degradation (Fig. 7). At the same time, the volumetric degradation showed the core's considerable role in protecting the fibril's

mechanical integrity. Furthermore, differently from surface degradation, the toughness of the fibril decreased dramatically with the increase in the rate of degradation. This finding supported the theory that the fibril's structural morphology is key to maintaining its toughness (Fratzl, 2008). Thus, the observed deterioration of the mechanical properties of the fibril led to the existence of a critical degradation amount that compromised the whole fibril mechanical integrity. The difference in the number of compromised molecules could explain the differential reaction of the fibril to the surface and volumetric degradation mechanism. In the case of surface degradation, the initial deterioration of the fibril led to breaking some molecular surface chains and, therefore, disabling these molecules' stretching capability. Additional degradation did not lead to additional breaking of new molecules since most molecules on the surface could no longer contribute to the tensile strength. However, additional degradation led to eliminating some parts of the molecules' contribution to the sliding resistance, which had less impact on the mechanical properties. In the case of volume degradation, the disabling of the sliding capabilities of molecules was not observed until most of the molecules in the fibril were already broken, leading to a sharper decay in mechanical properties.

The continuum simulated results indicated a consistent pattern shift in the stress-strain behaviour across degradation levels and mechanisms from what molecular level predictions were made. However, a clear difference in stress-strain magnitude was computed between the two levels (fibril and tissue levels). This difference indicated the key role of the non-collagenous matrix in producing a realistic aggregate mechanical reaction at the tissue level even when the collagenous component is compromised enzymatically (Bertassoni and

Swain, 2014; Cavalcante *et al.*, 2005). While having a determined explanation for the role of the non-collagenous matrix on the mechanical response of the soft tissue at different scales, further work and a more realistic representation of its components are needed (Hascall and Lowther, 1982; Zitnay and Weiss, 2018). On the side of the model verification, the direct comparison of the predicted results with experimentally or computationally published studies was difficult due to the multi-domain technique used during the present investigation (molecular dynamics and continuum mechanics), difference in the ACL geometry, constitutive formulation and examined parameters. Nevertheless, the ACL model's predicted elastoplastic stress-strain behaviour with native fibril (non-degraded) was very similar to experimental measurements [Butler *et al.*, 1986; Cooper *et al.*, 2007; Marieswaran *et al.*, 2018; Van Dommelen *et al.*, 2005; Yamamoto *et al.* (2003) Strain-rate dependence of mechanical failure properties of rabbit MCL and ACL. In: Proceedings of the Summer Bioengineering Conference, Key Biscayne, pp: 25-29, conference abstract] (Fig. 12**c**). This behaviour was characterised by a relatively large elongation followed by a linear and yielding response during gradual increases of the applied load before the complete failure of the structure. In addition, the computed tangent modulus of the linear region (388 MPa), tensile strength (58.9 MPa) and ultimate strain (12.5 %) were in the reported range of the experimental measurements (Butler *et al.*, 1986; Butler *et al.*, 1980; Kwan and Woo, 1989; Noyes *et al.*, 1974; Tohyama and Yasuda, 2011) (Table 6). For both degradation types, the elastic aggregate response of the ACL was significantly affected. For example, 33 % and 61 % decrease in the tangent modules was computed with 0.6 %

surface and volume degradation, respectively. The collagen surface degradation had a less devastating effect on the elastoplastic response of the ACL compared to the volume degradation. The latter significantly decreased the elastic stiffness of the ACL by reducing the yielding strain of the tissue by ~ 25 %, while elastic stiffness was almost unaffected by surface degradation. Also, the model predictions indicated a near 30 % additional reduction in the ACL capacity to support failure stress at 0.6 % volume degradation compared with the same percentage of surface degradation. One possible explanation for this differential effect was that the tropocollagen molecules on the superficial layer of fibril were randomly cleaved during surface degradation, resulting in an asymmetrical or irregular load transfer through superficial molecules. In contrast, the volume degradation affected the core of the fibril, which is mainly responsible for structure load bearing, and hence compromised the fibril and tissue stiffness. On the side of the ACL stress distribution, native and both degraded fibril scenarios resulted in stress concentration localised on the posterolateral bundle of the ACL near the tibial junction. This result was clearly corroborated by the experimental measurements of load distribution on the ACL bundles at full extension (Bach and Hull, 1998; Bach *et al.*, 1997; Woo *et al.*, 1998). This elastic stress dwindled in magnitude (~ 50 %) and not in the distribution area in both degradation mechanisms. The possible reason behind this observation was that the tissue stress was significantly more affected by the fibril degradation than the strain. The above prediction demonstrated first the validity of the proposed multidomain frame to estimate the physiological stress on the ACL and, second, the detrimental role
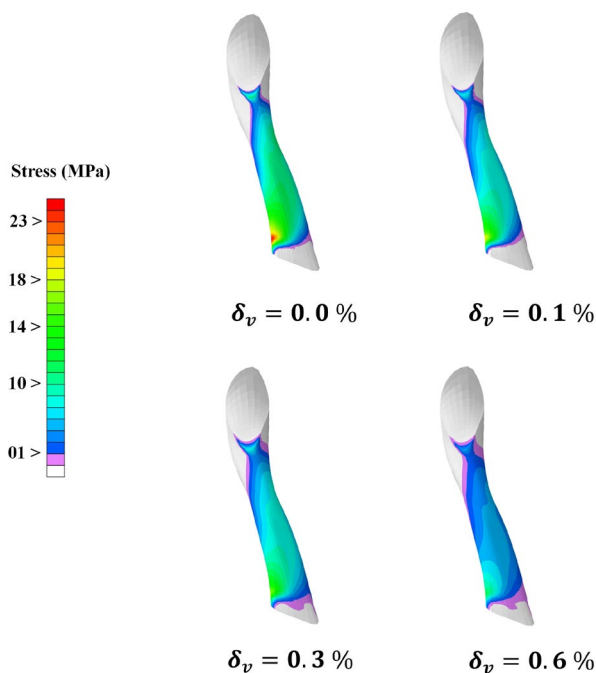

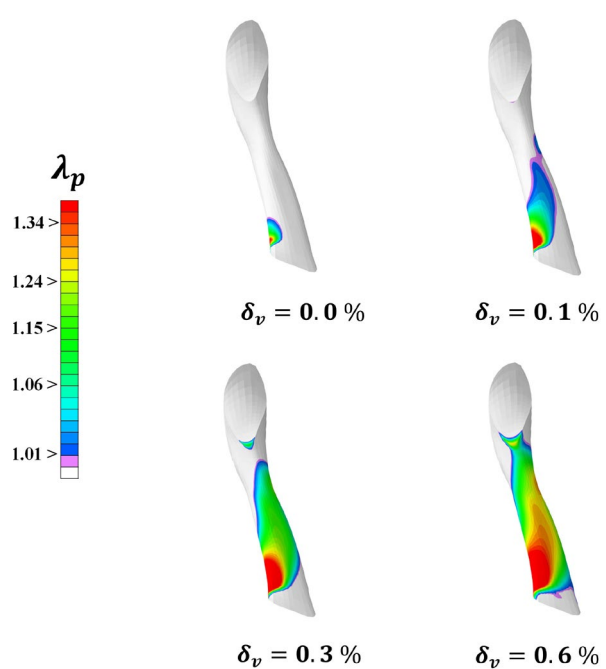**Fig. 10. Computed stress distribution in the ACL at 7.5 % axial strain (elastic zone) as a function of volumetric (δ_v) degradation.**

Fig. 11. Computed ACL damage distribution (plastic change) at 3 % post-yielding strain as a function of volumetric (δ_v) degradation.

of the enzymatical degradation mechanism in the reduced elastic capacity of the tissue. The alteration of ACL stress sustainability may clearly affect the main role of this ligament in the knee joint. This role is well documented as a principal constraint for anterior translation and as a secondary restraint for frontal and transversal rotations. Thus, the decrease in the tissue toughness by means of molecular degradation

Fig. 12. Predicted results verification. Comparison of present study and computed fibril normalised stress-strain (normalisation was performed relative to the maximum value) under (**a**) surface and (**b**) volume degradation (Malaspina *et al.*, 2017). (**c**) Comparison of present study and measured ACL axial stress during the tensile test [Butler *et al.*, 1986; Cooper *et al.*, 2007; Marieswaran *et al.*, 2018; Van Dommelen *et al.*, 2005; Yamamoto *et al.* (2003) Strain-rate dependence of mechanical failure properties of rabbit MCL and ACL. In: Proceedings of the Summer Bioengineering Conference, Key Biscayne, pp: 25-29, conference abstract].

will increase the laxity of the joint and the rotational instability in the coupled planes (frontal-transversal) (Adouni *et al.*, 2020; 2012).

The spatial distribution of the plastic changes (damage) of the ACL was presented in terms of fibril plastic elongation (λ_p). This plastic elongation is activated once the fibril stress reaches its point of yielding, hence, playing an important role in presenting the tissue damage initiation and propagation. Therefore, the spatial distribution between the two mechanisms of collagen degradation resembled in the initiation and propagation. The ACL damage was initiated from the posterolateral region near the tibial junction and spanned anteromedially in an average direction of 45° to the horizontal plane. The initiation of the ACL damage in a native fibril (non-degraded) required almost 59 MPa as axial stress, while in the cases of the degraded fibril, this value was significantly decreased to 40 and 15 MPa (Fig. 6). Thus, the less observed stresses to initiate the ACL plastic change may explain the expansion of the damage over the ligament structure. Furthermore, except for the two last simulated cases of volume degradation (0.3 and 0.6 %), the damage expansion was limited to the superficial layer of the ligament (2 layers of hex elements) and not transmitted to the deep layer. The non-uniformity of the cross-sectional area of the ACL and the higher area of the junction to the tibial and femoral bones that are associated with non-consistency of the collagen network orientations between layers may explain this surface damage locus (Riley, 2004; Weiss and Gardiner, 2001). However, in advanced volume degradation, since the complete collapsed area of damage (red area) was much larger, the fibril's loadbearing capacity almost vanished and simultaneous transmission of plastic change to the subsequent layer happened. The plastic change distribution observed in the present study was consistent with previous studies reporting ACL failure patterns (Bates *et al.*, 2018; Blaker *et al.*, 2017; Hsu H, 2019; Levine *et al.*, 2012; Noyes *et al.*, 1974; Noyes, 2012; Schenck Jr *et al.*, 1999; Viidik, 1968) and indicating that soft tissue damage starts typically at the superficial layer and propagates to the deep layers (Paschos *et al.*, 2010; Weiss and Gardiner, 2001).

Most ACL or even other soft tissue studies modelled the biomechanical response due to load-induced changes (Maas *et al.*, 2016; Marieswaran *et al.*, 2018; Quatman, 2009). Despite the great ability of this type of modelling technique (load-induced) to be directly validated, verified and cross-verified, a significant variation has been observed in the predicted ACL behaviour and mainly failure stress-strain. For example, the tensile failure stress of ACL ranges from 23 MPa to 83 MPa (Benos *et al.*, 2020; Birch *et al.*, 2013; Butler *et al.*, 1986; Homyk *et al.*, 2012; Paschos *et al.*, 2010). This variation may be attributed to many factors related to the used validation data [such as ligament maturation, ageing, gender, unseen micro defects or model assumptions (Weiss and Gardiner, 2001)] while, in the present study, the
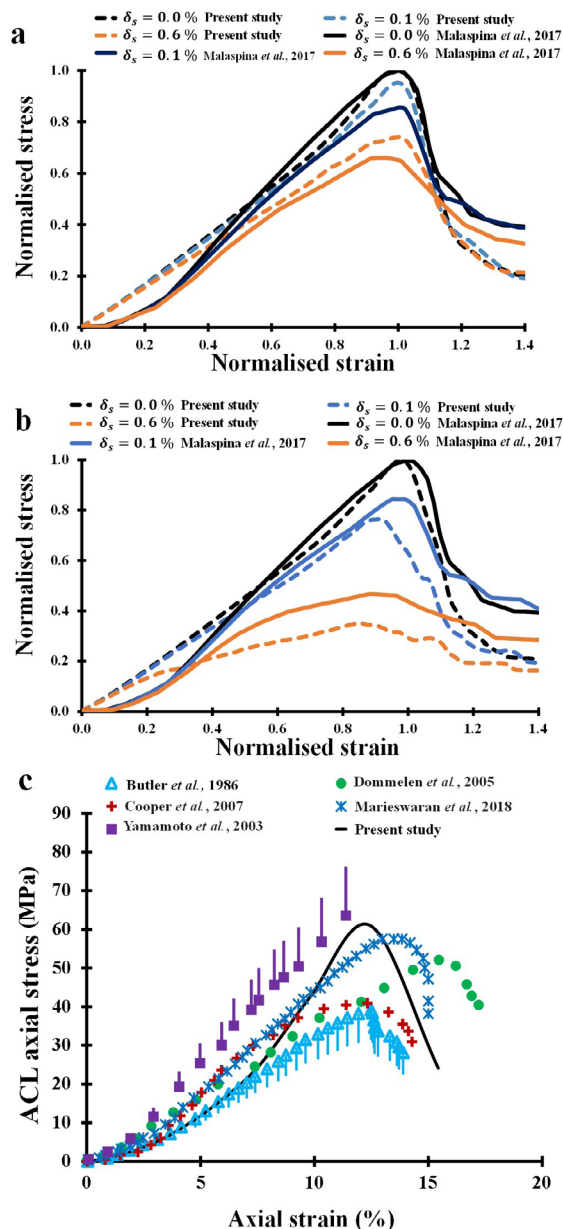
aggregate mechanical behaviour of the ACL was predicted using a bottom-up approach in the context of the fibril mechanic changes due to the enzymatical exposure. This novelty may be added as an additional factor that explains the difference between the current prediction and others. However, the current model can be employed for studying certain clinical aspects treating female gender bias ACL injury. Recent investigations have highlighted the potential role of the unbalanced enzymatical activity (higher level of collagen degradation) in female subjects before and after the menses period in the increased risk of ACL damage (Ireland, 2002; Powell *et al.*, 2015; Slauterbeck and Hardy, 2001). Besides, this model could be used to study other collagen molecular defects, such as the non-enzymatical linkage between tropocollagen molecules (Couppe *et al.*, 2009).

The present study presented several limitations. The components that may play a more important role in the fibril matrix, such as non-collagenous proteins, were not considered (Nanci, 1999). The fibril's surface and volume degradation, associated with collagenase treatment, was implemented using the Langmuir surface adsorption model. The study hypothesis was that enzyme adsorption probability to every ACL fibril was equal, leading to a similar degradation state of the tissue across layers (Powell *et al.*, 2015), while degradation mediated by enzymatical activity depends on many factors such as diffusion of the enzymes, fibril-matrix interaction and fibril surface with localised and higher stress concentration (Powell *et al.*, 2019). The characterisation of the failure of the proteoglycan network (matrix) was not considered. However, it remains to be seen if the inclusion of a hybrid model of degradation (fibril-matrix) will lead to a different mechanical behaviour. On the aggregate side, the predicted mechanical behaviour remains limited to the transient response of the tissues. Finally, the cases 1 % and 2 % of volumetric degradations were not simulated with the ACL model due to convergence issues.

The present study explored the mechanical response of the ACL by introducing molecular dynamics simulation of fibril enzymatically mediated degradation. The mechanism of degradation substantially and deferentially influenced the aggregate ACL behaviour. This is, to the best of the authors' knowledge, the first engineering frame in which a hybrid multi-domain model (molecular and continuum) was used to provide insight into the mechanics of ACL as a function of basic building block elements. Finally, this model can help a better understanding of the ACL injury mechanisms and associated risk factors that may affect current preventive, surgical and rehabilitation strategies.

References

Abrahams M (1967) Mechanical behaviour of tendon *in vitro*. Med Biol Eng **5**: 433-443.

Adouni M, Faisal TR, Dhaher YY (2020) Computational frame of ligament *in situ* strain in a full knee model. Comput Biol Med **126**: 104012. DOI: 10.1016/j.compbiomed.2020.104012.

Adouni M, Mbarki R, Al Khatib F, Eilaghi A (2021) Multiscale modeling of knee ligament biomechanics. Int J Numer Method Biomed Eng **37**: e3413. DOI: 10.1002/cnm.3413.

Adouni M, Shirazi-Adl A, Shirazi R (2012) Computational biodynamics of human knee joint in gait: from muscle forces to cartilage stresses. J Biomech **45**: 2149-2156.

Akizuki S, Mow VC, Müller F, Pita JC, Howell DS, Manicourt DH (1986) Tensile properties of human knee joint cartilage: I. Influence of ionic conditions, weight bearing, and fibrillation on the tensile modulus. J Orthop Res **4**: 379-392.

Asaro RJ, Rice J (1977) Strain localization in ductile single crystals. J Mech Phys Solids **25**: 309-338.

Bach JM, Hull ML (1998) Strain inhomogeneity in the anterior cruciate ligament under application of external and muscular loads. J Biomech Eng **120**: 497-503.

Bach JM, Hull ML, Patterson HA (1997) Direct measurement of strain in the posterolateral bundle of the anterior cruciate ligament. J Biomech **30**: 281-283.

Bates NA, Schilaty ND, Nagelli CV, Krych AJ, Hewett TE (2018) Validation of noncontact anterior cruciate ligament tears produced by a mechanical impact simulator against the clinical presentation of injury. Am J Sports Med **46**: 2113-2121.

Belytschko T, Liu WK, Moran B, Elkhodary K (2014) Nonlinear finite elements for continua and structures. Wiley.

Benos L, Stanev D, Spyrou L, Moustakas K, Tsaopoulos DE (2020) A review on finite element modeling and simulation of the anterior cruciate ligament reconstruction. Front Bioeng Biotechnol **8**: 967. DOI: 10.3389/fbioe.2020.00967.

Bertassoni LE, Swain MV (2014) The contribution of proteoglycans to the mechanical behavior of mineralized tissues. J Mech Behav Biomed Mater **38**: 91-104.

Birch HL, Thorpe CT, Rumian AP (2013) Specialisation of extracellular matrix for function in tendons and ligaments. Muscles Ligaments Tendons J **3**: 12-22.

Blaker CL, Little CB, Clarke EC (2017) Joint loads resulting in ACL rupture: effects of age, sex, and body mass on injury load and mode of failure in a mouse model. J Orthop Res **35**: 1754-1763.

Buehler MJ (2006) Nature designs tough collagen: explaining the nanostructure of collagen fibrils. Proc Natl Acad Sci U S A **103**: 12285-12290.

Buehler MJ (2008) Nanomechanics of collagen fibrils under varying cross-link densities: atomistic and continuum studies. J Mech Behav Biomed Mater **1**: 59-67.

Buehler MJ, Ballarini R (2013) Materiomics: multiscale mechanics of biological materials and structures. Springer-Verlag Wien.

Butler DL, Kay MD, Stouffer DC (1986) Comparison of material properties in fascicle-bone units from human patellar tendon and knee ligaments. J Biomech **19**: 425-432.

Butler DL, Noyes FR, Grood ES (1980) Ligamentous restraints to anterior-posterior drawer in the human knee. A biomechanical study. J Bone Joint Surg Am **62**: 259-270.

Catanese III J, Iverson EP, Ng RK, Keaveny TM (1999) Heterogeneity of the mechanical properties of demineralized bone. J Biomech **32**: 1365-1369.

Cavalcante FSA, Ito S, Brewer K, Sakai H, Alencar AM, Almeida MP, José S. Andrade J, Majumdar A, Ingenito EP, Suki B (2005) Mechanical interactions between collagen and proteoglycans: implications for the stability of lung tissue. J Appl Physiol (1985) **98**: 672-679.

Chang SW, Shefelbine SJ, Buehler MJ (2012) Structural and mechanical differences between collagen homo- and heterotrimers: relevance for the molecular origin of brittle bone disease. Biophysical J **102**: 640-648.

Connolly ML (1983) Solvent-accessible surfaces of proteins and nucleic acids. Science **221**: 709-713.

Cooper JA, Sahota JS, Gorum WJ, Carter J, Doty SB, Laurencin CT (2007) Biomimetic tissue-engineered anterior cruciate ligament replacement. Proc Natl Acad Sci U S A **104**: 3049-3054.

Couppe C, Hansen P, Kongsgaard M, Kovanen V, Suetta C, Aagaard P, Kjaer M, Magnusson SP (2009) Mechanical properties and collagen cross-linking of the patellar tendon in old and young men. J Appl Physiol (1985) **107**: 880-886.

DeBotton G, Hariton I, Socolsky E (2006) Neo-Hookean fiber-reinforced composites in finite elasticity. J Mech Phys Solids **54**: 533-559.

Depalle B, Qin Z, Shefelbine SJ, Buehler MJ (2015) Influence of cross-link structure, density and mechanical properties in the mesoscale deformation mechanisms of collagen fibrils. J Mech Behav Biomed Mater **52**: 1-13.

Depalle B, Qin Z, Shefelbine SJ, Buehler MJ (2016a) Large deformation mechanisms, plasticity, and failure of an individual collagen fibril with different mineral content. J Bone Miner Res **31**: 380-390.

Depalle B, Qin Z, Shefelbine SJ, Buehler MJ (2016b) Large deformation mechanisms, plasticity, and failure of an individual collagen fibril with different mineral content. J Bone Miner Res **31**: 380-390.

Diamant J, Keller A, Baer E, Litt M, Arridge R (1972) Collagen; ultrastructure and its relation to mechanical properties as a function of ageing. Proc R Soc Lond B Biol Sci **180**: 293-315.

Erdemir A (2016) Open knee: open source modeling & simulation to enable scientific discovery and clinical care in knee biomechanics. J Knee Surg **29**: 107-116.

Fang M, Holl MMB (2013) Variation in type I collagen fibril nanomorphology: the significance and origin. BoneKEy Rep **2**: 394. DOI: 10.1038/bonekey.2013.128.

Fratzl P (2008) Collagen: structure and mechanics, an introduction. Springer Science & Business Media. pp: 1-13.

Frobell RB, Lohmander LS, Roos HP (2007) Acute rotational trauma to the knee: poor agreement between clinical assessment and magnetic resonance imaging findings. Scand J Med Sci Sports **17**: 109-114.

Gasser TC, Holzapfel GA (2002) A rate-independent elastoplastic constitutive model for biological fiber-reinforced composites at finite strains: continuum basis, algorithmic formulation and finite element implementation. Computational Mechanics **29**: 340-360.

Gautieri A, Redaelli A, Buehler MJ, Vesentini S (2014) Age- and diabetes-related nonenzymatic crosslinks in collagen fibrils: candidate amino acids involved in advanced glycation end-products. Matrix Biol **34**: 89-95.

Gautieri A, Vesentini S, Redaelli A, Buehler MJ (2011) Hierarchical structure and nanomechanics of collagen microfibrils from the atomistic scale up. Nano Lett **11**: 757-766.

Georgiev GP, Landzhov B, Kotov G, Slavchev SA, Iliev A (2018) Matrix metalloproteinase-2 and -9 expression in the epiligament of the medial collateral and anterior cruciate ligament in human knees: a comparative study. Cureus **10**: e3550-e3550.

Guo ZY, Caner F, Peng XQ, Moran B (2008) On constitutive modelling of porous neo-Hookean composites. J Mech Phys Solids **56**: 2338-2357.

Guo ZY, Peng XQ, Moran B (2006) A composites-based hyperelastic constitutive model for soft tissue with application to the human annulus fibrosus. J Mech Phys Solids **54**: 1952-1971.

Hascall VC, Lowther DA (1982) Components of the organic matrix: proteoglycans. In: Proceedings of the Biological Mineralization and Demineralization. Berlin, Heidelberg. pp: 179-198.

Homyk A, Orsi A, Wibby S, Yang N, Nayeb-Hashemi H, Canavan PK (2012) Failure locus of the anterior cruciate ligament: 3D finite element analysis. Comput Methods Biomech Biomed Engin **15**: 865-874.

Hsu H, Siwiec RM (2019) Patellar tendon rupture. StatPearls [Internet].

Ireland ML (2002) The female ACL: why is it more prone to injury? Orthop Clin North Am **33**: 637-651.

Kwan MK, Woo SL (1989) A structural model to describe the nonlinear stress-strain behavior for parallel-fibered collagenous tissues. J Biomech Eng **111**: 361-363.

Lee EH (1969) Elastic-plastic deformation at finite strains. J Appl Mech **36**: 1-6.

Levine JW, Kiapour AM, Quatman CE, Wordeman SC, Goel VK, Hewett TE, Demetropoulos CK (2012) Clinically relevant injury patterns after an anterior cruciate ligament injury provide insight into injury mechanisms. Am J Sports Med **41**: 385-395.

Liu Y, Thomopoulos S, Chen C, Birman V, Buehler MJ, Genin GM (2014) Modelling the mechanics of partially mineralized collagen fibrils, fibres and tissue. J R Soc Interface **11**: 20130835. DOI: 10.1098/rsif.2013.0835.

Lorenzo AC, Caffarena ER (2005) Elastic properties, Young's modulus determination and structural stability of the tropocollagen molecule: a computational study by steered molecular dynamics. J Biomech **38**: 1527-1533.

Maas SA, Erdemir A, Halloran JP, Weiss JA (2016) A general framework for application of prestrain to computational models of biological materials. J Mech Behav Biomed Mater **61**: 499-510.

Malaspina DC, Szleifer I, Dhaher Y (2017) Mechanical properties of a collagen fibril under simulated degradation. J Mech Behav Biomed Mater **75**: 549-557.

Marieswaran M, Jain I, Garg B, Sharma V, Kalyanasundaram D (2018) A review on biomechanics of anterior cruciate ligament and materials for reconstruction. Appl Bionics Biomech **2018**: 14. DOI: 10.1155/2018/4657824.

McLean SG, Mallett KF, Arruda EM (2015) Deconstructing the anterior cruciate ligament: what we know and do not know about function, material properties, and injury mechanics. J Biomech Eng **137**: 020906. DOI: 10.1115/1.4029278.

Myklebust G, Bahr R (2005) Return to play guidelines after anterior cruciate ligament surgery. Br J Sports Med **39**: 127-131.

Nanci A (1999) Content and distribution of noncollagenous matrix proteins in bone and cementum: relationship to speed of formation and collagen packing density. J Struct Biol **126**: 256-269.

Nikolov S, Raabe D (2008) Hierarchical modeling of the elastic properties of bone at submicron scales: the role of extrafibrillar mineralization. Biophys J **94**: 4220-4232.

Noyes FR, Torvik PJ, Hyde WB, Delucas JL (1974) Biomechanics of ligament failure: II. An analysis of immobilization, exercise, and reconditioning effects in primates. JBJS **56**: 1406-1418.

Noyes SB-WDF (2012) ACL injury rehabilitation: everything you need to know to restore knee function and return to activity. Noyes Knee Institute, Cincinnati, USA.

Ochi M, Shino K, Yasuda K, Kurosaka M (2016) ACl injury and its treatment. Springer.

Orgel JP, Irving TC, Miller A, Wess TJ (2006) Microfibrillar structure of type I collagen *in situ*. Proc Natl Acad Sci U S A **103**: 9001-9005.

Paschos NK, Gartzonikas D, Barkoula N-M, Moraiti C, Paipetis A, Matikas TE, Georgoulis AD (2010) Cadaveric study of anterior cruciate ligament failure patterns under uniaxial tension along the ligament. Arthroscopy **26**: 957-967.

Perumal S, Antipova O, Orgel JP (2008) Collagen fibril architecture, domain organization, and triple-helical conformation govern its proteolysis. Proc Natl Acad Sci U S A **105**: 2824-2829.

Plimpton S (1995) Fast parallel algorithms for short-range molecular dynamics. J Comput Physics **117**: 1-19.

Powell B, Malaspina DC, Szleifer I, Dhaher Y (2019) Effect of collagenase-gelatinase ratio on the mechanical properties of a collagen fibril: a combined Monte Carlo-molecular dynamics study. Biomech Model Mechanobiol **18**: 1809-1819.

Powell BS, Dhaher YY, Szleifer IG (2015) Review of the multiscale effects of female sex hormones on matrix metalloproteinase-mediated collagen degradation. Crit Rev Biomed Eng **43**: 401-428.

Quatman CE (2009) Anterior cruciate ligament injury mechanisms in female athletes: a finite element investigation. The University of Toledo.

Riley G (2004) Tendon and ligament biochemistry and pathology. Soft Tissue Rheumatology **2053**: 3-39.

Saito M, Marumo K, Fujii K, Ishioka N (1997) Single-column high-performance liquid chromatographic-fluorescence detection of immature, mature, and senescent cross-links of collagen. Anal Biochem **253**: 26-32.

Sanders TL, Maradit Kremers H, Bryan AJ, Larson DR, Dahm DL, Levy BA, Stuart MJ, Krych AJ (2016) Incidence of anterior cruciate ligament tears and reconstruction: a 21-year population-based study. Am J Sports Med **44**: 1502-1507.

Schenck Jr RC, Kovach IS, Agarwal A, Brummett R, Ward RA, Lanctot D, Athanasiou KA (1999) Cruciate injury patterns in knee hyperextension: a cadaveric model. Arthroscopy **15**: 489-495.

Schilaty ND, Nagelli C, Bates NA, Sanders TL, Krych AJ, Stuart MJ, Hewett TE (2017) Incidence of second anterior cruciate ligament tears and identification of associated risk factors from 2001 to 2010 using a geographic database. Orthop J Sports Med **5**: 2325967117724196. DOI: 10.1177/2325967117724196.

Shen ZL, Dodge MR, Kahn H, Ballarini R, Eppell SJ (2008) Stress-strain experiments on individual collagen fibrils. Biophysical J **95**: 3956-3963.

Shen ZL, Kahn H, Ballarini R, Eppell SJ (2011) Viscoelastic properties of isolated collagen fibrils. Biophysical J **100**: 3008-3015.

Slauterbeck JR, Hardy DM (2001) Sex hormones and knee ligament injuries in female athletes. Am J Med Sci **322**: 196-199.

Snedeker JG, Gautieri A (2014) The role of collagen crosslinks in ageing and diabetes - the good, the bad, and the ugly. Muscles Ligaments Tendons J **4**: 303-308.

Song Y, Debski RE, Musahl V, Thomas M, Woo SLY (2004) A three-dimensional finite element model of the human anterior cruciate ligament: a computational analysis with experimental validation. J Biomech **37**: 383-390.

Stevens MJ (2008) Simulation of the mechanical strength of a single collagen molecule. Biophysical J **95**: 33-39.

Stukowski A (2009) Visualization and analysis of atomistic simulation data with OVITO–the open visualization tool. Modelling Simul Mater Sci Eng **18**: 015012. DOI: 10.1088/0965-0393/18/1/015012.

Sweeney SM, Orgel JP, Fertala A, McAuliffe JD, Turner KR, Di Lullo GA, Chen S, Antipova O, Perumal S, Ala-Kokko L (2008) Candidate cell and matrix interaction domains on the collagen fibril, the predominant protein of vertebrates. J Biol Chem **283**: 21187-21197.

Takeuchi M, Kikuchi S, Sasaki N, Suzuki T, Watai T, Iwaki M, Bucala R, Yamagishi S-i (2004) Involvement of advanced glycation end-products (AGEs) in Alzheimer's disease. Curr Alzheimer Res **1**: 39-46.

Tang H, Buehler MJ, Moran B (2009a) A constitutive model of soft tissue: from nanoscale collagen to tissue continuum. Ann Biomed Eng **37**: 1117-1130.

Tang H, Buehler MJ, Moran B (2009b) A constitutive model of soft tissue: from nanoscale collagen to tissue continuum. Ann Biomed Eng **37**: 1117-1130.

Tang Y, Ballarini R, Buehler MJ, Eppell SJ (2010) Deformation micromechanisms of collagen fibrils under uniaxial tension. J R Soc Interface **7**: 839-850.

Tang Z, Yang L, Xue R, Zhang J, Wang Y, Chen PC, Sung KP (2009c) Differential expression of matrix metalloproteinases and tissue inhibitors of metalloproteinases in anterior cruciate ligament and medial collateral ligament fibroblasts after a mechanical injury: Involvement of the p65 subunit of NF-κB. Wound Repair Reg **17**: 709-716.

Tohyama H, Yasuda K (2011) Application of growth factors for enhancement of mechanical strength of grafted tendon following anterior cruciate ligament reconstruction. IntechOpen. DOI: 10.5772/21185.

Van Dommelen JA, Ivarsson B, Jolandan MM, Millington SA, Raut M, Kerrigan JR, Crandall JR, Diduch D (2005) Characterization of the rate-dependent mechanical properties and failure of human knee ligaments. SAE Transactions: 80-90.

Vasan S, Zhang X, Zhang X, Kapurniotu A, Bernhagen J, Teichberg S, Basgen J, Wagle D, Shih D, Terlecky I (1996) An agent cleaving glucose-derived protein crosslinks *in vitro* and *in vivo*. Nature **382**: 275-278.

Viidik A (1968) Elasticity and tensile strength of the anterior cruciate ligament in rabbits as influenced by training. Acta Physiol Scand **74**: 372-380.

Watanabe-Nakayama T, Itami M, Kodera N, Ando T, Konno H (2016) High-speed atomic force microscopy reveals strongly polarized movement of clostridial collagenase along collagen fibrils. Sci Rep **6**: 1-11.

Weiss JA, Gardiner JC (2001) Computational modeling of ligament mechanics. Crit Rev Biomed Eng **29**: 303-371.

Wenger MP, Bozec L, Horton MA, Mesquida P (2007) Mechanical properties of collagen fibrils. Biophysical J **93**: 1255-1263.

Woo SLY, Fox RJ, Sakane M, Livesay GA, Rudy TW, Fu FH (1998) Biomechanics of the ACL: measurements of *in situ* force in the ACL and knee kinematics. Knee **5**: 267-288.

Zitnay JL, Weiss JA (2018) Load transfer, damage, and failure in ligaments and tendons. J Orthop Res **36**: 3093-3104.

Web Reference

1. https://simtk.org/projects/openknee

Discussion with Reviewer

Reviewer: Apart from homogenisation to scale up the properties from molecular level to continuum level, what are other techniques to do so?

Authors: Different approaches can be used to understand the hierarchical-mechanical response of a soft tissue. A simple post-processing method can be employed as an alternative to computational homogenisation. This technique involves the numerically obtained macro-scale behaviour (possibly using FE analysis) to generate boundary conditions of micro-scale models that are solved to compute the micro-scale response. However, a weaker coupling between scales that must satisfy multiple assumptions about hierarchies' consistency should be respected. The independence between scales is one of the major advantages of this technique. Besides, the inclusion of micro-scale elements into the macro-scale model represents the least abstracted technique. However, this approach requires the assembly of small volumes and, hence, a tremendous number of elements, with a too high computational cost given the present technology.

Editor's note: The Guest Editor responsible for this paper was Dimitrios Zeugolis.